



Observing the Redshifted 21 cm Signal around a Bright QSO at $z \sim 10$

Qing-Bo Ma^{1,2} , Benedetta Ciardi³, Koki Kakiichi⁴ , Saleem Zaroubi^{5,6,7}, Qi-Jun Zhi^{1,2}, and Philipp Busch³¹ School of Physics and Electronic Science, Guizhou Normal University, Guiyang 550001, People's Republic of China; maq@gznu.edu.cn² Guizhou Provincial Key Laboratory of Radio Astronomy and Data Processing, Guizhou Normal University, Guiyang 550001, People's Republic of China³ Max-Planck-Institut für Astrophysik, Karl-Schwarzschild-Straße 1, D-85748 Garching bei München, Germany⁴ Department of Physics and Astronomy, University College London, London WC1E 6BT, UK⁵ Kapteyn Astronomical Institute, University of Groningen, P.O. Box 800, NL-9700 AV Groningen, The Netherlands⁶ Department of Natural Sciences, Open University of Israel, 1 University Road, P.O. Box 808, Ra'anana 4353701, Israel⁷ Department of Physics, The Technion, Haifa 32000, Israel

Received 2019 June 13; revised 2019 November 16; accepted 2019 November 24; published 2020 January 15

Abstract

We use hydrodynamics and radiative transfer simulations to study the 21 cm signal around a bright QSO at $z \sim 10$. Due to its powerful UV and X-ray radiation, the QSO quickly increases the extent of the fully ionized bubble produced by the pre-existing stellar type sources, in addition to partially ionizing and heating the surrounding gas. As expected, a longer QSO lifetime, t_{QSO} , results in a 21 cm signal in emission located at increasingly larger angular radii, θ , and covering a wider range of θ . Similar features can be obtained with a higher galactic emissivity efficiency, f_{UV} , such that determining the origin of a large ionized bubble (i.e., QSO versus stars) is not straightforward. Such degeneracy could be reduced by taking advantage of the finite light travel time effect, which is expected to affect an H II region produced by a QSO differently from one created by stellar type sources. From an observational point of view, we find that the 21 cm signal around a QSO at various t_{QSO} could be detected by Square Kilometre Array1-low instrument with a high signal-to-noise ratio (S/N). As a reference, for $t_{\text{QSO}} = 10$ Myr, a $\text{S/N} \sim 8$ is expected assuming that no pre-heating of the intergalactic medium has taken place due to high- z energetic sources, while it can reach values above 10 in cases of pre-heating. Observations of the 21 cm signal from the environment of a high- z bright QSO could then be used to set constraints on its lifetime, as well as to reduce the degeneracy between f_{UV} and t_{QSO} .

Unified Astronomy Thesaurus concepts: Quasars (1319); High-redshift galaxies (734); Radiative transfer (1335); Reionization (1383)

1. Introduction

After the formation of the first structures in the universe (see Ciardi & Ferrara 2005; Bromm 2013; Dayal & Ferrara 2018 for reviews), their UV and X-ray radiation started to propagate into the surrounding neutral gas and initiate the reionization process, which should be complete by $z \simeq 6$, as suggested by the Gunn–Peterson trough in QSO spectra (Fan et al. 2006a, 2006b, but see e.g., Kulkarni et al. 2019 for a recent discussion on the possibility of having a later reionization). This era is referred to as the epoch of reionization (EoR). Cosmic microwave background experiments, most recently the *Planck* telescope, measured a Thomson scattering optical depth $\tau = 0.0544 \pm 0.007$ (Planck Collaboration et al. 2018), suggesting a global ionization fraction of 0.5 at redshift 7.68 ± 0.79 . However, more details on the EoR are expected from 21 cm experiments, such as the Low-Frequency Array (LOFAR),⁸ the Murchison Widefield Array,⁹ the Hydrogen Epoch of Reionization Array,¹⁰ and the upcoming Square Kilometre Array (SKA).¹¹

Although the first sources (e.g., metal-free stars and mini-QSOs) are predicted to have bright radiation that initiates and contributes to the reionization process (Chen & Miralda-Escudé 2008; Ghara et al. 2016), they cannot provide the full photon budget required to complete reionization (Choudhury &

Ferrara 2006; Trac & Cen 2007). The bulk of H-ionizing photons are instead produced by subsequent stellar generations, together with minor contributions from more energetic sources such as X-ray binaries (XRB), QSOs, and shock-heated interstellar medium (ISM; Dijkstra et al. 2004; Eide et al. 2018). While any single one of these sources is typically too faint to be detected (but refer also to Ghara et al. 2016, 2017 for a more optimistic view), their integral contribution could be measured by 21 cm experiments, e.g., in terms of 21 cm power spectra (e.g., Madau et al. 1997; Geil & Wyithe 2009; Christian & Loeb 2013; Patil et al. 2014; Seiler et al. 2018; Ross et al. 2019), 21 cm bispectra (e.g., Shimabukuro et al. 2017; Watkinson et al. 2019), and cross-correlations of 21 cm with other observations (e.g., Vrbancic et al. 2016; Ma et al. 2018; Moriawaki et al. 2019). An exception is constituted by sources as bright as QSOs that carve large ionized regions (Alvarez & Abel 2007; Feng et al. 2013; Kakiichi et al. 2017), which could be resolved by 21 cm telescopes (Geil et al. 2008; Majumdar et al. 2011; Datta et al. 2012, 2016; Bolgar et al. 2018), and possibly used to set constraints on the ionizing photon rate and/or lifetimes of the quasar (Wyithe & Loeb 2004; Datta et al. 2012), as well as to distinguish a reionization history dominated by QSOs from one dominated by stellar type sources (e.g., Hassan et al. 2019). These bright sources could also be directly detected by optical/near-infrared telescopes such as the Thirty Meter Telescope, the Euclid telescope, and the *James Webb Space Telescope* (JWST). Combining information from such different observations is expected to offer the possibility of a more thorough investigation of the ionizing and

⁸ <http://www.lofar.org/>⁹ <http://www.mwatelescope.org/>¹⁰ <https://reionization.org/>¹¹ <https://www.skatelescope.org/>

heating processes of the intergalactic medium (IGM), as well as of the source properties during the EoR.

In this paper, we study the 21 cm signal associated with a bright QSO at $z \sim 10$ using the simulations described in Kakiichi et al. (2017, hereafter K17), and the detectability of such a signal with LOFAR and SKA. Incidentally, this is within the range of redshift of the LOFAR peak performance, i.e., $z \sim 8.5\text{--}10.5$ (Patil et al. 2017). As mentioned earlier, similar works appeared in the literature, employing both analytic models (e.g., Wyithe & Loeb 2004; Majumdar et al. 2011) and radiative transfer (RT) simulations (e.g., Datta et al. 2012; Bolgar et al. 2018). Building on these, K17 has run a suite of 3D cosmological N -body/hydrodynamical and multi-frequency RT simulations to model the QSO environment (i.e., the surrounding galaxies and the intergalactic medium), the spectral shape of the radiation emitted by the QSO as well as the galaxies, and the propagation of such radiation with a consistent treatment of UV and X-ray photons, and secondary ionization. Here we will present an investigation of the 21 cm signal around the high- z bright QSO investigated in K17.

The cosmological parameters adopted are from the *Wilkinson Microwave Anisotropy Probe* 9 yr result (Hinshaw et al. 2013): $\Omega_\Lambda = 0.74$, $\Omega_m = 0.26$, $\Omega_b = 0.0463$, $h = 0.72$, $n_s = 0.95$ and $\sigma_8 = 0.85$. The layout of the paper is as follows. Section 2 describes the simulations adopted. The expected 21 cm signal and signal-to-noise ratio (S/N) are in Section 3. The conclusions and discussions are in Section 4.

2. Simulations

For this study we adopt the simulations discussed in K17. Here we outline the features relevant to this work, while we refer the reader to the original paper for more details.

As a first step, the IGM and galaxies were modeled by running the smoothed particle hydrodynamics code GADGET-3 (Springel 2005) until $z = 10$, with 2×512^3 dark matter and gas particles. The simulation box has a length of $50 h^{-1}$ cMpc and it is by design centered on the largest halo, with a mass $M_{\text{halo}} = 1.34 \times 10^{10} h^{-1} M_\odot$ at $z = 10$.

Then, the gas density and temperature were mapped onto a Cartesian grid with 256^3 cells, to be used as input for the RT code CRASH (Ciardi et al. 2001; Maselli et al. 2003, 2009; Graziani et al. 2013, 2018), which models the gas temperature and ionization (of both its H and He components) by following the propagation of ionizing photons in the frequency range 13.6 eV–2 keV. The stellar type sources hosted by galaxies were turned on at $z = 15$, with an ionizing photon rate linearly related to the halo mass:

$$\dot{N}_{\text{ion}}^{\text{GAL}}(M_{\text{halo}}) = \dot{n}_{\text{ion}}(z) \frac{M_{\text{halo}}}{\bar{\rho}_{\text{halo}}}, \quad (1)$$

where $\bar{\rho}_{\text{halo}} = \sum_{j=1}^{N_s} M_{\text{halo}}^j / V_{\text{box}}$,

$$\dot{n}_{\text{ion}}(z) = 10^{50.89} \lambda(z) \frac{\alpha_b + 3}{2\alpha} f_{\text{UV}}, \quad (2)$$

V_{box} is the comoving volume of the simulation box, N_s denotes the total number of galaxies from the simulation, α (α_b) is the power-law spectral index of the sources (the ionizing background), $\lambda(z)$ describes the redshift dependence of the star formation rate density, and f_{UV} is the emissivity efficiency. α and α_b are assumed to be 3. The adopted expression for

$\lambda(z) = \frac{\xi e^{\zeta(z-9)}}{\xi - \zeta + \zeta e^{\zeta(z-9)}}$ with $\xi = 14/15$ and $\zeta = 2/3$ is from Bolton & Haehnelt (2007) and Ciardi et al. (2012). Considering the uncertainty in galactic luminosities and escape fraction during the EoR, three f_{UV} values have been adopted, i.e., $f_{\text{UV}} = 0.05, 0.1$, and 0.2 , which are in the range allowed by current experiments. For each of the three simulations, another was run in which a QSO located in the most massive halo in the center of the box, which was turned on at $z = 10$ for a time $t_{\text{QSO}} = 10$ Myr, i.e., until $z = 9.85$. Its ionizing photon production rate was modeled by rescaling the properties of ULAS J1120+0641 (Bolton et al. 2011; Mortlock et al. 2011) at $z = 7.085$ to $z = 10$, i.e., $\dot{N}_{\text{ion}}^{\text{QSO}} = 1.36 \times 10^{56}$ photons s^{-1} . We assumed its spectrum to be a power law $L_\nu^{\text{QSO}}(\nu) \propto \nu^{-1.5}$ and its radiation to be spherically symmetric.

A total of six simulations are included in this paper, three with and three without the QSO contribution. In K17 they are named GAL_R+QSO_UVXsec (our fiducial model, which includes the effect of the QSO and adopts $f_{\text{UV}} = 0.1$), GAL_0.5R+QSO_UVXsec, GAL_2R+QSO_UVXsec, GAL_R, GAL_0.5R, and GAL_2R.

Finally, large-scale simulations like those considered here are affected by resolution contamination in the cells containing the ionization front (I-front). When stars are the only sources of radiation, the I-front is expected to be very sharp due to the small mean-free path of the UV photons, thus it cannot be resolved. As a consequence, the cells that contain it appear as partially ionized and warm (Ross et al. 2017), while in reality part of the gas in the cell should be neutral and cold, and part fully ionized and hot. As this issue can affect the estimate of the 21 cm signal, we correct for it using a post-processing technique that exploits knowledge about the dominance of stellar emission in fully ionized regions and the negligible width (compared to the cell dimension) of the corresponding I-front.

More specifically, we divide each partially ionized cell into n_{sub} (in this work 8; we have checked that a value of 64 gives the same results) sub-cells that are either fully ionized or completely neutral.¹² Assigning to all sub-cells the same density of the original cell, the number of fully ionized sub-cells, n_{ion} , is

$$n_{\text{ion}} = \text{round}(x_{\text{H II}} \cdot n_{\text{sub}}), \quad (3)$$

where $x_{\text{H II}}$ is the ionization fraction of the original cell. This procedure also assures that the average ionization fraction of the sub-cells closely matches that of the original cell.

To decide which sub-cells will be fully ionized or fully neutral, we minimize their distance to fully ionized cells by calculating the Euclidean distance transform (Rosenfeld & Pfaltz 1966) and choosing the n_{ion} sub-cells with the smallest distance. We iterate this process until it converges, usually after two to four iterations. This procedure leaves us with compact arrangements of sub-cells that smoothly trace the original borders. The temperature in the ionized sub-cells is set to the temperature of the parent cell, while in the neutral ones it is set to the value from the original hydrodynamical simulation. Note that although this method is likely to underestimate the temperature of the ionized sub-cells, as they do not contribute

¹² Note that, for consistency in the analysis, also fully ionized/neutral cells can be equally refined, but the sub-cells in this case have the same physical properties of the original cells.

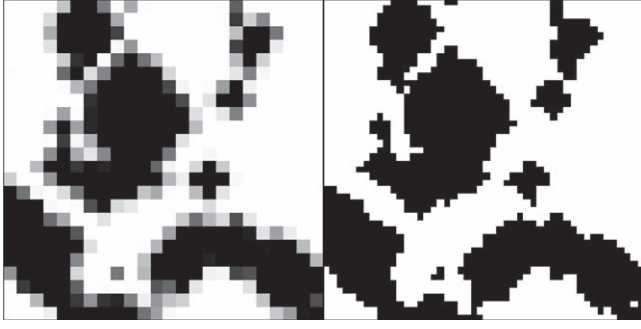


Figure 1. Example slice of an ionization field before (left panel) and after (right panel) our correction procedure as described in Section 2. The grayscale map gives the ionization field in linear units with black representing fully ionized and white representing completely neutral. The splitting of one layer of cells into eight sub-cells per cell results in two layers of sub-cell, of which we are only showing one in this example.

to the emission of the 21 cm signal, our assumption does not affect the final results.

An example of the outcome in terms of the ionization field produced by stellar type sources is given in Figure 1, where we show a slice of the field before and after the correction procedure described above. We clearly see that the partially ionized cells (gray cells in the left panel) are now split into fully neutral/ionized sub-cells.

The procedure is slightly different when radiation beyond the UV range is present, as harder photons indeed lead to extended, partially ionized, warm regions. In these cases the first layer of partially ionized cells outside fully ionized regions is corrected by setting their ionization level and temperature to those of the closest cell not in direct contact with fully ionized regions and therefore only affected by the long mean-free path radiation.

3. Results

In this section we will evaluate the 21 cm signal expected from the QSO environment, as well as discuss its detectability.

3.1. Expected 21 cm Signal

The brightness temperature of the 21 cm signal can be expressed as (Furlanetto et al. 2006)

$$\delta T_{21\text{ cm}} = 27\text{ mK} \times x_{\text{HI}}(1 + \delta) \left(1 - \frac{T_{\text{CMB}}}{T_s}\right) \times \left(\frac{1+z}{10} \frac{0.15}{\Omega_m h^2}\right)^{1/2} \left(\frac{\Omega_b h^2}{0.023}\right), \quad (4)$$

where x_{HI} is the fraction of neutral hydrogen, δ is the gas overdensity, T_{CMB} is the CMB temperature, and T_s is the spin temperature, for which we make the reasonable assumption that it is fully coupled to the gas temperature T at the redshifts of interest. In the following, we will consider two cases: one in which the only sources of heating are those included in our simulations, i.e., $T_s = T$, and a second one in which we assume that the IGM is preheated in the early stages of cosmic reionization by more energetic sources like nuclear black holes, XRB and/or shock-heated ISM (see e.g., Eide et al. 2018), i.e., $T_s \gg T_{\text{CMB}}$. We have tested how peculiar velocities affect our results using the MM-RRM (Mesh-to-Mesh Real-to-Redshift-Space-Mapping) method described in Mao et al. (2012) to

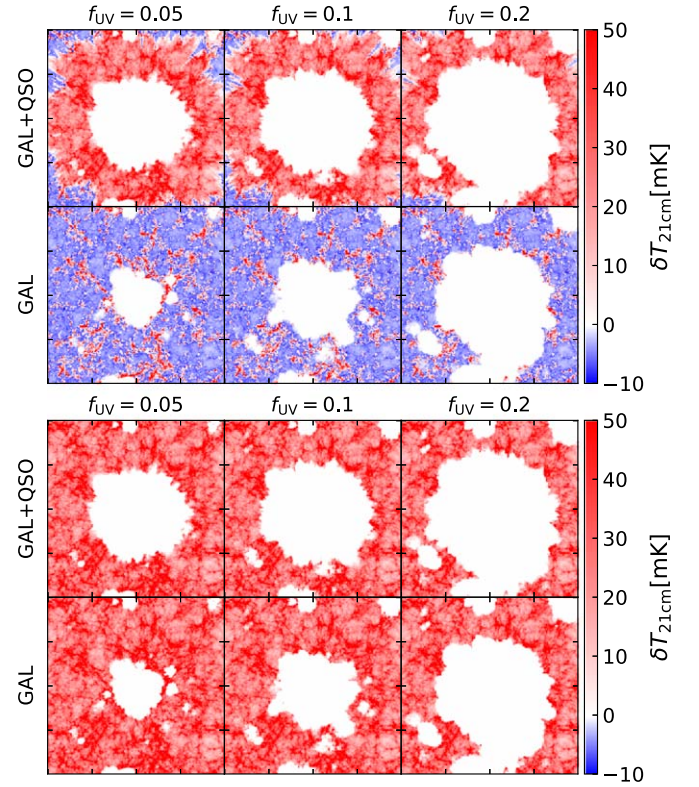


Figure 2. Top figure: central slices of 21 cm signal from the simulations with (upper panels) and without (lower panels) QSOs in the case of $T_s = T$. From left to right the columns refer to $f_{\text{UV}} = 0.05, 0.1$, and 0.2 . The length of each axis is $50 h^{-1}$ cMpc. The maps refer to $t_{\text{QSO}} = 10$ Myr ($z = 9.85$). Bottom figure: same as the top except that $T_s \gg T_{\text{CMB}}$.

include redshift space distortions. As we find that this correction has an effect at a percentage level, we ignore it in the remainder of the paper to simplify the discussion.

Figure 2 shows the central slices of the 21 cm signal around the QSO for $t_{\text{QSO}} = 10$ Myr (corresponding to $z = 9.85$ and an observed frequency of $\nu = 130.9$ MHz), together with the results of simulations without QSOs. As already discussed in K17, the presence of a bright QSO increases the extent of the fully ionized region, although its effect becomes less evident with increasing f_{UV} (i.e., galactic luminosity). On the other hand, because of the longer mean-free path of the more energetic photons emitted (which extend into the soft X-ray regime), the presence of a QSO is characterized by a ring of warm and partially ionized gas, which is absent when only stellar type sources are considered. In the case of $T_s = T$, this results in a strong positive 21 cm signal just outside the fully ionized region, while it is much smaller in simulations without QSO. Note that in the later case the positive 21 cm signal is due to the shockwave heating modeled in the hydrodynamic simulation. If we are instead in a regime in which $T_s \gg T_{\text{CMB}}$, the 21 cm signal is always positive. Compared to simulations with only stellar sources, the maps with a QSO have no obvious feature indicating its presence, except for the slightly larger size of the ionized bubble.

Figure 3 shows the spherically averaged 21 cm signal for $t_{\text{QSO}} = 10$ Myr as a function of the angular radius θ with the simulation box center as the zero-point, i.e., the 21 cm signal distribution around the central halo hosting the QSO. The top panel presents the results assuming $T_s = T$ for the simulations including only galaxies (thin lines) and both galaxies and the

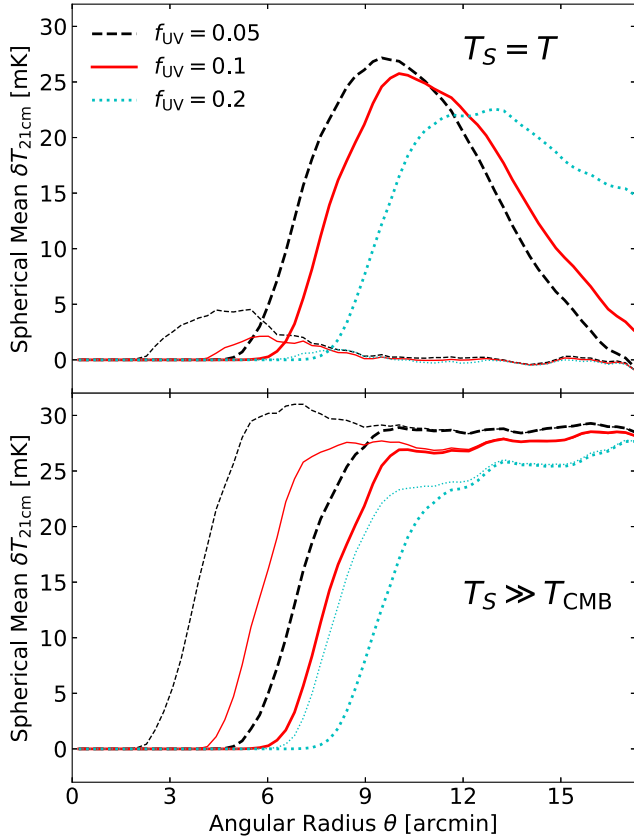


Figure 3. Spherically averaged 21 cm signal from the simulations with (thick lines) and without (thin lines) QSO. The lines refer to $f_{\text{UV}} = 0.05$ (black dashed), 0.1 (red solid), and 0.2 (cyan dotted). The top and bottom panels refer to the case with $T_S = T$ and $T_S \gg T_{\text{CMB}}$, respectively. The profiles are shown for $t_{\text{QSO}} = 10$ Myr ($z = 9.85$).

QSO (thick lines), for three different values of f_{UV} . With only galaxies, the 21 cm signal is always much weaker ($\delta T_{21\text{ cm}} < 5$ mK) than with the inclusion of the QSO. As mentioned earlier, the signal in emission is due to shock-heated gas and thus is roughly proportional to the gas density. As a consequence, the amplitude of the signal outside the ionized bubble decreases with increasing radius. For the same reason, the simulation with higher f_{UV} produces a larger ionized bubble and thus a lower 21 cm amplitude. In the simulation with both galaxies and QSO, the presence of the QSO manifests itself as a strong emission peak corresponding to the partially ionized ring observed in the previous figure, with the highest value of $\delta T_{21\text{ cm}} \sim 27$ mK reached at $\theta \sim 9.5'$ in the simulation with $f_{\text{UV}} = 0.05$. The UV emitting efficiency f_{UV} not only relates to the size of ionized bubbles, but also affects the amplitude and distribution of the average 21 cm signal. For example, if f_{UV} is increased to 0.1 and 0.2, the location of the peak shifts to larger angular radii, i.e., to $\theta \sim 10'$ and $13'$, respectively. Meanwhile, the intensity of the peak decreases to $\delta T_{21\text{ cm}} \sim 22.5$ mK and ~ 20 mK, since a higher f_{UV} leads to a lower mean n_{HI} in the partially ionized ring.

The bottom panel presents the same results with $T_S \gg T_{\text{CMB}}$. In this case, the amplitude of the 21 cm signal is proportional to $x_{\text{HI}}(1 + \delta)$, thus the signal is always positive, increasing rapidly outside the fully ionized region and reaching a value of $\delta T_{21\text{ cm}} \sim 27$ mK independently from the presence of the QSO. The only effect of the QSO is that, by increasing the size of the ionized bubble, it pushes the emission to larger radii. While this

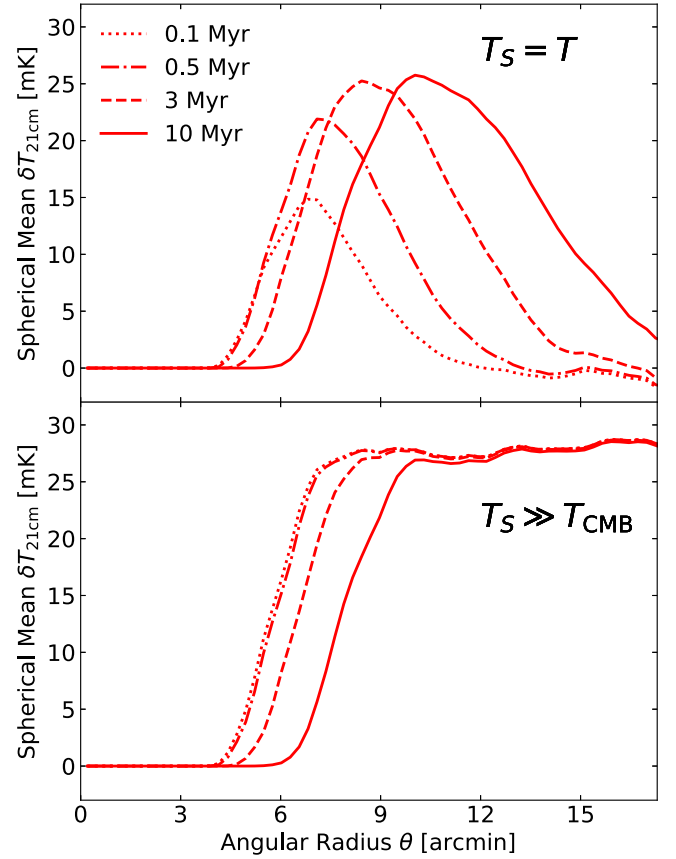


Figure 4. Spherically averaged 21 cm signal from our fiducial model with $t_{\text{QSO}} = 0.1$ Myr (dotted), 0.5 Myr (dashed-dotted), 3 Myr (dashed), and 10 Myr (solid). The top and bottom panels refer to the case with $T_S = T$ and $T_S \gg T_{\text{CMB}}$, respectively.

is more evident for lower values of f_{UV} , for which the profiles are more dissimilar, they nevertheless do not present any characteristic that would point toward the presence of a QSO. In fact, results from simulations with only more luminous stellar sources could be very similar to those with a QSO and lower f_{UV} (e.g., the thin cyan dotted and thick red solid lines in the bottom panel of Figure 3), while larger f_{UV} usually give lower values of $\delta T_{21\text{ cm}}$ because of the lower n_{HI} , similarly to what is observed for $T_S = T$.

Figure 4 shows the spherically averaged 21 cm signal in the fiducial model for various ages of the QSO. The 21 cm signal with $T_S = T$ shows obvious evolution in a short time, with the peak of the emission moving quickly away from the central source. Due to its high energy radiation, the QSO can quickly (i.e., less than 0.1 Myr) heat the surrounding gas well above T_{CMB} and induce a signal in emission. As t_{QSO} increases, both the fully ionized bubble and the range of angular radii ($\Delta\theta$) of positive 21 cm signal rapidly grow in size (e.g., $\Delta\theta$ is $\sim 8'$ at $t_{\text{QSO}} = 3$ Myr while $\sim 12'$ at $t_{\text{QSO}} = 10$ Myr). The enlarging ionized bubble is also clearly visible in 21 cm signal with $T_S \gg T_{\text{CMB}}$. In this case, the signal converges at large distances from the central source. Our results, for both assumptions on T_S , confirm previous suggestions (see e.g., Datta et al. 2012) that the rapid evolution of the 21 cm signal caused by a QSO could be used to constrain its age.

Majumdar et al. (2011) suggested that the finite light travel time (FLTT) effect is expected to affect the observed 21 cm signal from an H II region produced by a QSO much more

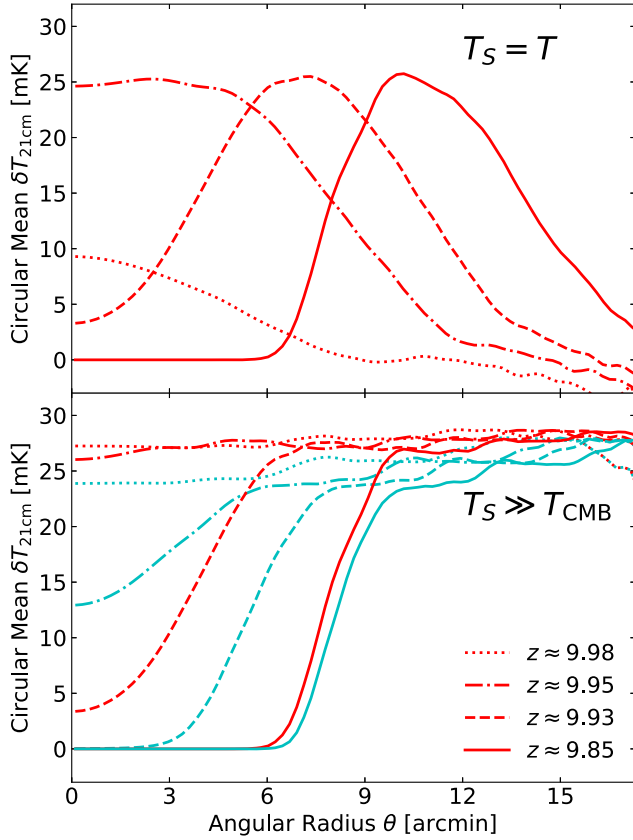


Figure 5. Circularly averaged 21 cm signal in slices perpendicular to the line of sight to the QSO at $z = 9.85$ in our fiducial model. The slices correspond to $z = 9.98$ (dotted), 9.95 (dashed-dotted), 9.93 (dashed), and 9.85 (solid lines), i.e., $\nu = 129.3, 129.7, 130.0$, and 130.9 MHz. The top and bottom panels refer to the case with $T_S = T$ and $T_S \gg T_{\text{CMB}}$, respectively. The bottom panel also includes the results from the model without QSO but $f_{\text{UV}} = 0.2$ (thin cyan lines).

significantly than one by galaxies. More specifically, the observed 21 cm signal around a QSO is expected to be very anisotropic along the line of sight (LOS; Majumdar et al. 2011; Zawada et al. 2014), while that from only stellar sources would be more spherical. As a consequence, measuring the 21 cm signal along the LOS could be used to disentangle its origin. Additionally, as already discussed, a 21 cm signal similar to the one produced by a QSO with a given t_{QSO} could be obtained also by galaxies alone with an appropriate value of f_{UV} (see Figure 3). On the other hand, as the evolution in the case of a QSO is much more rapid, observations along the LOS to the QSO should reveal a signal different than from that in the case of galaxies only, and thus might be used to break the degeneracy between t_{QSO} and f_{UV} .

To test how the 21 cm signal behaves for our QSO model by considering the FLTT effect, Figure 5 shows the circularly averaged 21 cm signal of slices perpendicular to the LOS to the QSO of $t_{\text{QSO}} = 10$ Myr ($z = 9.85$) in our fiducial model. The slices refer to $z = 9.98, 9.95$, and 9.93 (i.e., $\nu = 129.3, 129.7$, and 130.0 MHz) that have comoving distances of 30, 22.8, and 16.6 Mpc to the QSO.¹³ With $T_S = T$, the 21 cm positive signal extends to $z = 9.98$, although at this redshift it is much weaker than that at lower redshift. While the characteristic ring

of 21 cm emission associated with the presence of a large bubble carved by the QSO is clearly visible until $z = 9.93$, with a peak at $\theta \sim 7.3$, at $z > 9.95$ it disappears. With $T_S \gg T_{\text{CMB}}$, only the 21 cm signal at $z \lesssim 9.93$ shows the features of an ionized bubble, while the signal at higher z resembles very closely that of the neutral gas medium.

To investigate if indeed the FLTT effect can reduce the degeneracy between f_{UV} and t_{QSO} when $T_S \gg T_{\text{CMB}}$, in the bottom panel of Figure 5 we also present the results from the model without QSO but $f_{\text{UV}} = 0.2$. As mentioned earlier, this case has a 21 cm signal at $z = 9.85$ similar to that of the fiducial model, but at $z = 9.93$ and 9.95 it displays an obviously lower signal at $\theta < 6'$. Farther away from the central source, e.g., at $z = 9.98$, the 21 cm signal is equivalent to one from an almost fully neutral IGM, i.e., an almost constant value with increasing θ , both with and without the QSO.

3.2. Detectability of the 21 cm Signal

In this section we investigate the feasibility of observing the 21 cm signal around the high- z QSO with radio interferometers like LOFAR and SKA1-low. The flux density noise of an interferometer can be expressed as (Wilson et al. 2009)

$$\sigma_S = \frac{2k_B T_{\text{sys}}}{\epsilon A_{\text{eff}} \sqrt{N_{\text{st}}(N_{\text{st}} - 1) B t_{\text{int}}}}, \quad (5)$$

where k_B is the Boltzmann constant, T_{sys} is the system temperature, ϵ is the efficiency factor, A_{eff} is the effective collecting area, N_{st} is the number of stations, B is the frequency bandwidth, and t_{int} is the integration time. $S = \epsilon A_{\text{eff}} / T_{\text{sys}}$ denotes the sensitivity of one station. Using the Rayleigh-Jeans relation $\sigma_S = 2k_B \Delta T_b \Omega_{\text{beam}} \lambda^{-2}$, the brightness temperature of the instrumental noise can then be expressed as

$$\delta T_N = \frac{\lambda^2}{S \Omega_{\text{beam}} \sqrt{N_{\text{st}}(N_{\text{st}} - 1) B t_{\text{int}}}}, \quad (6)$$

where $\Omega_{\text{beam}} = 1.133 \vartheta^2$ and ϑ is the angular resolution. Note that here we simply assume all the station pairs to have the same angular resolution, while the real distributions of stations of SKA1-low and LOFAR are scale-dependent (van Haarlem et al. 2013; Dewdney et al. 2016).

SKA1-low¹⁴ is designed to have 512 stations and expected to cover the frequency range 50–350 MHz (corresponding to a 21 cm signal at $3 \lesssim z \lesssim 27$). The sensitivity of each station is $S = 0.97 \text{ m}^2 \text{ K}^{-1}$ at $\nu = 130.9$ MHz ($z = 9.85$). Its baselines will be arranged in a compact core with a diameter of 1 km and longer baselines up to 80 km. An accurate noise calculation requires a realistic distribution of the antenna and the simulation of the uv-coverage. Here we follow Ghara et al. (2017) and simply assume an angular resolution $\vartheta = 2'$. It should be kept in mind that a higher/lower resolution would lead to larger/smaller noise on the images and thus lower/higher S/N, while a resolution that is too low would not be able to capture the details of the 21 cm signal around the QSO.

For LOFAR (see e.g., Ciardi et al. 2015), we assume $\epsilon = 0.5$, $N_{\text{st}} = 48$, $T_{\text{sys}} = [140 + 60(\nu/300 \text{ MHz})^{-2.55}] \text{ K}$ and $A_{\text{eff}} = \min\left(\frac{\lambda^2}{3}, 1.5626\right) \times 16 \times 24 \text{ m}^2$ (24 tiles times 16

¹³ Note that, since our RT simulations do not include the effects of finite speeds of ionizing photons, here we only consider the FLTT effect of the 21 cm photons that travel from the neutral hydrogen to the observer.

¹⁴ The parameters used here are taken from the SKA website <https://astronomers.skatelescope.org/>.

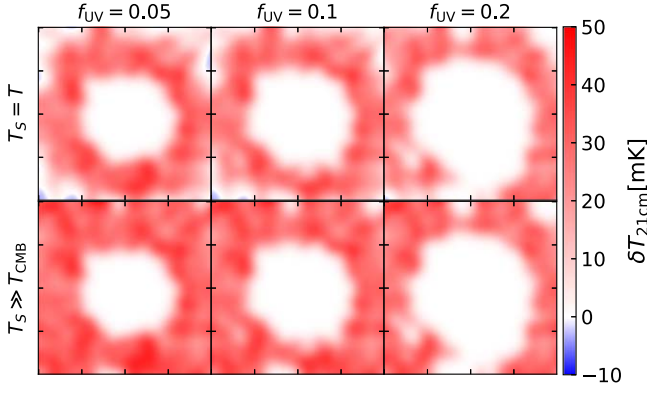


Figure 6. Central slices of 21 cm signal from the simulations with QSO in the case of $T_S = T$ (top) and $T_S \gg T_{\text{CMB}}$ (bottom). From left to right, the columns refer to $f_{\text{UV}} = 0.05, 0.1$, and 0.2 . The maps refer to $t_{\text{QSO}} = 10$ Myr (i.e., $z = 9.85$ and $\nu = 130.9$ MHz) and have been obtained assuming an angular resolution of $2'$. The thickness of the slices (3.8 Mpc) corresponds to a frequency band 0.2 MHz.

dipoles per tile for one core station). For consistency and a better comparison, also in this case we adopt $\vartheta = 2'$.

We assume that foreground contamination can be removed without any residual, thus we do not include the foreground noise (Geil et al. 2008). For both SKA1-low and LOFAR, we take an integration time $t_{\text{int}} = 3000$ hr and a frequency band $B = 0.2$ MHz corresponding to $\Delta z = 0.0166$ and a comoving length of 3.8 Mpc at $z = 9.85$. To mimic the real observations then, in the following discussion we only consider a slice of the simulation box centered around the QSO with a width corresponding to 0.2 MHz. To produce mock maps with pixel size $2'$, we additionally average the physical properties of the cells in bins of width corresponding to $2'$ (equivalent to 5.6 comoving Mpc at $z = 9.85$). The S/N along the angular radius can then be defined as $S/N = N_{\text{pixel}}^{1/2} \delta \bar{T}_{21\text{cm}} \delta T_N^{-1}$, where $\delta \bar{T}_{21\text{cm}}$ is the average signal in the pixels contained within a bin of width ϑ , and N_{pixel} is the number of pixels in the same bin.

Before discussing the detectability of the signal, in Figure 6 we show a sample of mock observed 21 cm maps produced with an angular resolution of $2'$. The maps refer to simulations including a QSO of $t_{\text{QSO}} = 10$ Myr, i.e., $z = 9.85$ and $\nu = 130.9$ MHz, with three different f_{UV} values, assuming both $T_S = T$ (upper panels) and $T_S \gg T_{\text{CMB}}$ (lower panels). The maps are obtained by summing the central slices in the simulation contained within a comoving length of 3.8 Mpc (corresponding to $B = 0.2$ MHz), and then smoothing the resulting map with a Gaussian kernel of $2'/(2\sqrt{2\ln 2})$, i.e., 2.38 Mpc. Compared to the theoretical maps in Figure 2, these mock observed maps show weaker fluctuations (as they are smoothed), while the central ionized bubble, as well as the emission from the heated IGM, are still clearly visible for both $T_S = T$ and $T_S \gg T_{\text{CMB}}$. We should note that it will be difficult to capture these features with the $8'$ resolution expected for the SKA1-low core.

Figure 7 shows the expected S/N of an observation of our reference QSO with $t_{\text{QSO}} = 10$ Myr both for SKA1-low and LOFAR. While with LOFAR the S/N is always < 1 , for SKA1-low S/N values above 1 are obtained in a wide range of θ , with a maximum of ~ 8 for $T_S = T$ and > 10 for $T_S = T_{\text{CMB}}$. At distances larger than the ionized bubbles the S/N for $T_S \gg T_{\text{CMB}}$ is much larger than that for $T_S = T$, due to the higher $\delta T_{21\text{cm}}$ (see Figure 3). While f_{UV} has little influence on

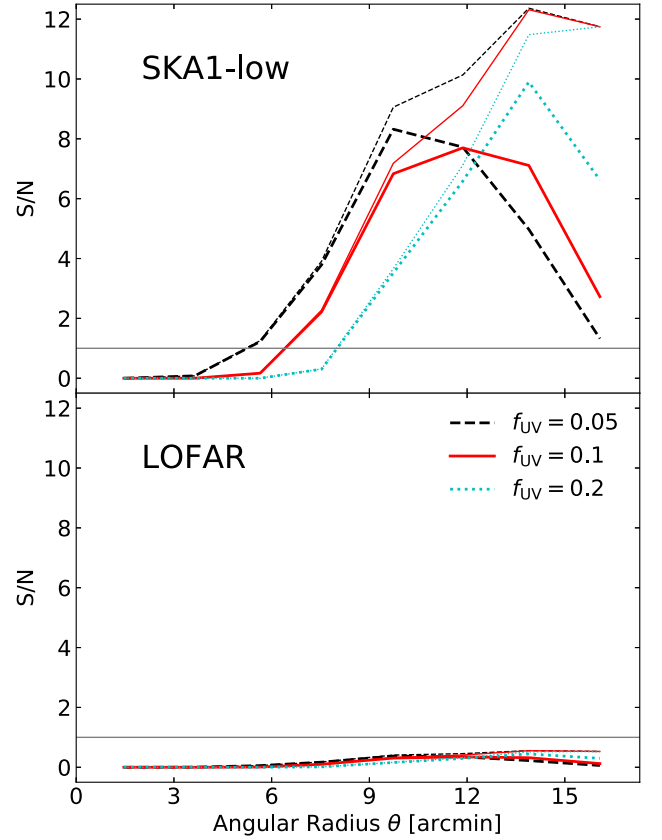


Figure 7. S/N expected from observations with SKA1-low (upper panel) and LOFAR (lower) in the simulations, with a QSO turning on at $z = 10$ and a lifetime of $t_{\text{QSO}} = 10$ Myr (i.e., $z = 9.85$ and $\nu = 130.9$ MHz). The different lines refer to galactic emissivities of $f_{\text{UV}} = 0.05$ (black dashed lines), 0.1 (red solid), and 0.2 (cyan dotted). The thick and thin lines refer to the cases with $T_S = T$ and $T_S \gg T_{\text{CMB}}$, respectively, while the horizontal line at $S/N = 1$ is drawn to guide the eye. The S/N has been calculated assuming a bandwidth $B = 0.2$ MHz, an integration time $t_{\text{int}} = 3000$ hr, and an angular resolution $\vartheta = 2'$.

the highest S/N attainable, larger luminosities shift the detection to higher values and a wider range of θ .

Figure 8 shows the expected SKA1-low S/N for our fiducial model at different t_{QSO} . With $T_S = T$, the highest S/N is ~ 3 at $t_{\text{QSO}} = 0.1$ Myr. As t_{QSO} increases, so does the S/N, and the signal from a wider range of θ can be detected. With $T_S \gg T_{\text{CMB}}$, the 21 cm signal outside of the ionized bubble could be detected with a high S/N (> 8 at $\theta > 8'$) for all the t_{QSO} considered here.

Figure 9 shows the expected SKA1-low S/N of slices perpendicular to the LOS at redshifts higher than the one of the QSO. For $T_S = T$, while the S/N is < 1 at $z = 9.98$, it can be > 5 at the other redshifts. The range of θ over which the signal is detectable extends to larger values with decreasing redshift. With $T_S \gg T_{\text{CMB}}$ the S/N is always > 1 in a wide range of θ at these redshifts.

We note that although LOFAR is not able to image the 21 cm signal around the QSO with $\vartheta = 2'$, it is possible to observe the signal with a lower angular resolution and still give a good measurement of its evolution along the LOS. For example, if we take $\vartheta = 12'$, which is enough to resolve the ionized bubble of the QSO in our fiducial simulation at $t_{\text{QSO}} = 10$ Myr (see, e.g., Figure 5), then the LOFAR noise is $= 11.4$ mK, giving an S/N at $z = 9.95, 9.93$, and 9.85 of 1.9, 1.7, and 0.06 if $T_S = T$, corresponding to an average

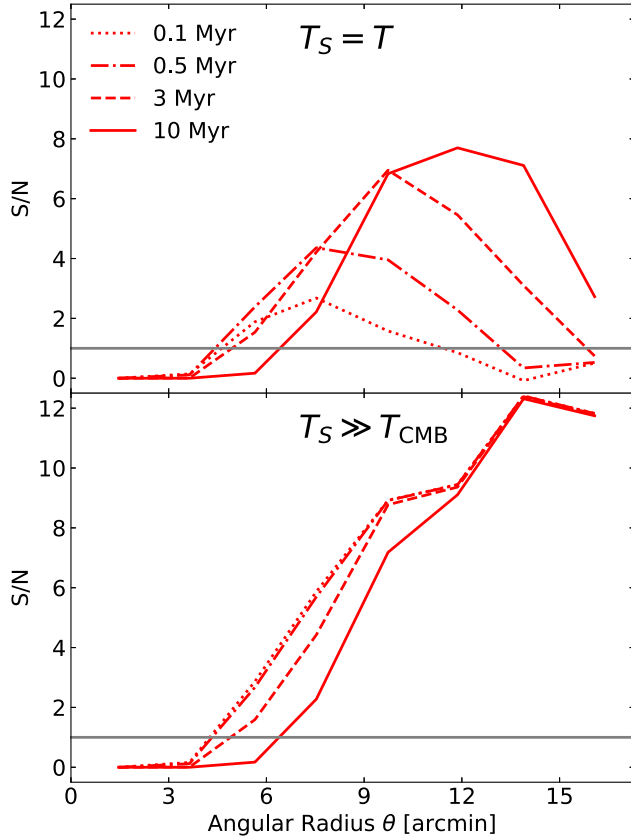


Figure 8. S/N expected from observations with SKA1-low in our fiducial model at $t_{\text{QSO}} = 0.1$ Myr (red dotted lines), 0.5 Myr (dashed-dotted), 3 Myr (dashed), and 10 Myr (solid). The top and bottom panels refer to the case with $T_S = T$ and $T_S \gg T_{\text{CMB}}$, respectively. The horizontal line at $S/N = 1$ is drawn to guide the eye. The S/N has been calculated assuming an angular resolution $\theta = 2'$, a bandwidth $B = 0.2$ MHz, and an integration time $t_{\text{int}} = 3000$ hr.

$\delta T_{21\text{ cm}} = 22, 19.9$ and 0.7 mK, respectively. The S/N would be 2.5, 1.8, and 0.06 if $T_S = T_{\text{CMB}}$, corresponding to an average $\delta T_{21\text{ cm}} = 29.1, 20.7$, and 0.7 mK, respectively.

4. Discussion and Conclusion

Although the abundance of QSOs is expected to decline with increasing redshift (e.g., Fan et al. 2001; Khandai et al. 2015), the possibility of detecting these very bright objects at $z \gtrsim 10$ with 21 cm line experiments is intriguing, as most hydrogen is expected to still be neutral at these high redshifts, and thus the impact of heating from energetic sources such as QSOs, XRBs, and shock-heated ISM should be at maximum (see, e.g., Eide et al. 2018), and be less relevant at lower z when the universe is highly ionized (Datta et al. 2012). Additionally, while the detection of a bubble ionized by a QSO could be used to set constraints on a QSO's characteristics, such as its ionizing photon rate and/or lifetime (see, e.g., Datta et al. 2012), resolving features associated with the QSO could become more challenging with decreasing redshift and merging of ionized regions (Furlanetto & Oh 2005). However, at lower z bright QSOs might also have significant effects on the surrounding 21 cm signal (Alvarez & Abel 2007; Geil et al. 2008), e.g., by affecting the morphology of the H II regions they are born in (Datta et al. 2012).

We analyze the results of hydrodynamical and radiative transfer (RT) simulations (Kakiichi et al. 2017) to study the 21 cm signal around a bright QSO at $z \sim 10$ and its

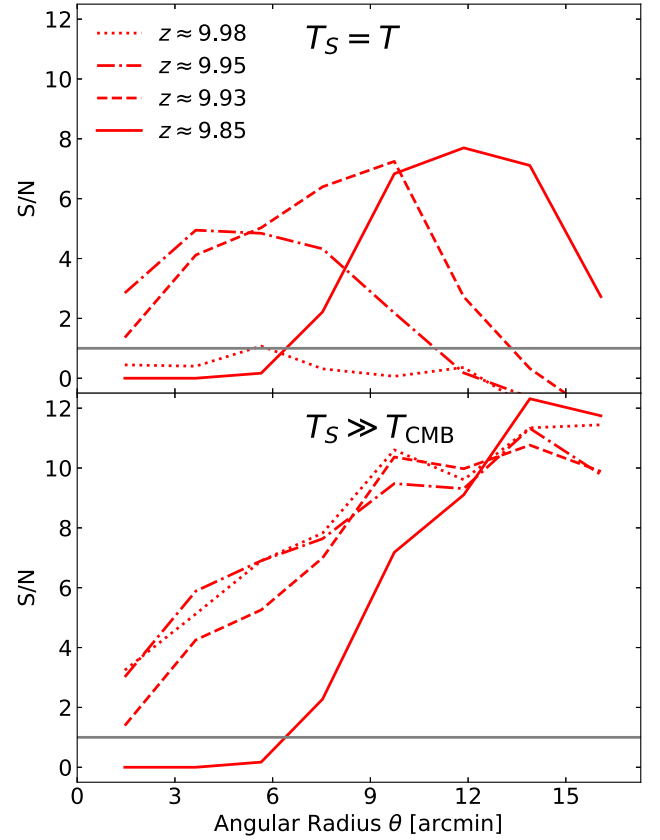


Figure 9. S/N expected from observations with SKA1-low of slices at $z = 9.98$ (dotted), $z = 9.95$ (dashed-dotted), and $z = 9.93$ (dashed) and $z = 9.85$ (solid) from the fiducial model with $t_{\text{QSO}} = 10$ Myr. The top and bottom panels refer to the case with $T_S = T$ and $T_S \gg T_{\text{CMB}}$, respectively. The horizontal line at $S/N = 1$ is drawn to guide the eye.

detectability with SKA1-low and LOFAR. The RT calculations include ionizing photons both from the QSO and the galaxies surrounding it. As a reference, we also present the results of RT with only galaxies. Additionally, for each case we have three simulations with different galaxy emissivity efficiencies, f_{UV} , to take into account the uncertainties of galactic luminosities and escape fraction during the epoch of reionization. Finally, to include the uncertainties of gas heating at $z \sim 10$, we consider a case in which the spin temperature, T_S , has the same value of the gas temperature, i.e., $T_S = T$, and another one for which $T_S \gg T_{\text{CMB}}$.

With the assumption that the radiation of the QSO is isotropic, our results for 21 cm signal show fairly spherically symmetric features. However, the emission direction of the radiation though depends on the structure of the QSO's inner regions, leading typically to an anisotropic flux (Elvis 2000). This could change the morphology of the ionized bubbles, as well as the distribution of the 21 cm emission signal. It should be noted, though, that such anisotropies would be partially washed out by the galaxies that also contribute abundant ionizing photons to the ionized region, thus most of our conclusions should still be applicable.

Because of its strong radiation, the QSO can quickly heat its surroundings to a temperature $T \gg T_{\text{CMB}}$, without fully ionizing the hydrogen component of the gas. As a consequence, we find that for a QSO's lifetime of $t_{\text{QSO}} = 10$ Myr (corresponding to $z = 9.85$), the spherically averaged 21 cm brightness temperature, $\delta T_{21\text{ cm}}$, in the case of $T_S = T$, displays

a peak with a typical amplitude of ~ 25 mK and angular radius $\theta \sim 10'$, the former decreasing and the latter increasing with increasing f_{UV} . For $T_S \gg T_{\text{CMB}}$ the 21 cm signal remains flat once $\delta T_{21\text{ cm}}$ reaches its peak, whose amplitude and angular radius exhibit the same dependence on f_{UV} with the case of $T_S = T$. As expected, the size of the ionized bubble and the radius of the 21 cm emission signal increase quickly with t_{QSO} , a feature that would aid the determination of the age of the QSO (Datta et al. 2012). Note that the measurement of both 21 cm images and the rate of ionizing photons of galaxies and QSO are necessary to determine the lifetime of the QSO (see the discussions in Datta et al. 2012). Such an exercise will be additionally complicated by e.g., the anisotropic emission of QSOs and the uncertainties in the QSO and galaxy luminosity (Euclid Collaboration et al. 2019), the latter increasing the error bar in the determination of the QSO lifetime. Although a detailed study of the impact of these quantities is beyond the scope of this paper, we believe that 3D measurements of the 21 cm signal should give a rough picture of the anisotropic emission of the QSO and suggest whether the QSO is observed at an early or late evolutionary stage.

We then investigate the detectability of the signal around the QSO with SKA1-low and LOFAR. At $z = 9.85$ (corresponding to $t_{\text{QSO}} = 10$ Myr and $\nu = 130.9$ MHz), with an integration time of 3000 hr and an angular resolution of $2'$, SKA1-low could reach an S/N of ~ 8 for $T_S = T$ and > 10 for $T_S \gg T_{\text{CMB}}$. This is always lower than 1 in the case of LOFAR, with the same integration time and angular resolution, while we find that with an angular resolution of $12'$, LOFAR is able to measure the 21 cm signal along the LOS with an S/N ~ 1 –2. For $t_{\text{QSO}} = 0.1$ –10 Myr the S/N for SKA1-low is expected to be larger than 1 in a wide range of angular radii. Once the size of the ionized bubble and the 21 cm emission signal are resolved, one could set constraints on the lifetime of QSOs. Note that with the matched filter technique discussed in Datta et al. (2012) an S/N higher than the one found in this work could be reached. As t_{QSO} affects the 21 cm signal around the QSO in a way similar to f_{UV} , an observation of the signal might not be able to break the degeneracy between these two parameters. Considering the effect of FLTT (Majumdar et al. 2011), such degeneracy could be reduced by measuring the 3D structure of the 21 cm signal, since the FLTT effect is expected to affect the 3D image of a signal around a QSO more than that around galaxies. As an example, we have an estimated expectation for our reference QSO at $z = 9.85$, finding that SKA1-low could reach S/N > 1 in a wide range of angular radii at redshifts as high as $z = 9.98$.

This work is supported by the innovation and entrepreneurial project of Guizhou province for high-level overseas talents (grant no. (2019)02), the National Natural Science Foundation of China (grants No. 11847075, 11903010, 11565010, and U1731218), and the Science and Technology Fund of Guizhou Province (grants No. (2015)4015, (2016)4008, (2017)5726–37, (2018)5769–02). The tools for bibliographic research are offered by the NASA Astrophysics Data Systems and by the JSTOR archive.

ORCID iDs

Qing-Bo Ma  <https://orcid.org/0000-0001-9493-4565>
Koki Kakiichi  <https://orcid.org/0000-0001-6874-1321>

References

- Alvarez, M. A., & Abel, T. 2007, *MNRAS*, **380**, L30
 Bolgar, F., Eames, E., Hottier, C., & Semelin, B. 2018, *MNRAS*, **478**, 5564
 Bolton, J. S., & Haehnelt, M. G. 2007, *MNRAS*, **382**, 325
 Bolton, J. S., Haehnelt, M. G., Warren, S. J., et al. 2011, *MNRAS*, **416**, L70
 Bromm, V. 2013, *RPPh*, **76**, 112901
 Chen, X., & Miralda-Escudé, J. 2008, *ApJ*, **684**, 18
 Choudhury, T. R., & Ferrara, A. 2006, *MNRAS*, **371**, L55
 Christian, P., & Loeb, A. 2013, *JCAP*, **9**, 014
 Ciardi, B., Bolton, J. S., Maselli, A., & Graziani, L. 2012, *MNRAS*, **423**, 558
 Ciardi, B., & Ferrara, A. 2005, *SSRv*, **116**, 625
 Ciardi, B., Ferrara, A., Marri, S., & Raimondo, G. 2001, *MNRAS*, **324**, 381
 Ciardi, B., Inoue, S., Abdalla, F. B., et al. 2015, *MNRAS*, **453**, 101
 Datta, K. K., Friedrich, M. M., Mellema, G., Iliev, I. T., & Shapiro, P. R. 2012, *MNRAS*, **424**, 762
 Datta, K. K., Ghara, R., Majumdar, S., et al. 2016, *JApA*, **37**, 27
 Dayal, P., & Ferrara, A. 2018, *PhR*, **780**, 1
 Dewdney, Stevenson, T. J., McPherson, A. M., et al. 2016, SKA1 SYSTEM BASELINE DESIGN V2, https://astronomers.skatelescope.org/wp-content/uploads/2016/05/SKA-TEL-SKO-0000002_03_SKA1SystemBaselineDesignV2.pdf
 Dijkstra, M., Haiman, Z., & Loeb, A. 2004, *ApJ*, **613**, 646
 Eide, M. B., Graziani, L., Ciardi, B., et al. 2018, *MNRAS*, **476**, 1174
 Elvis, M. 2000, *ApJ*, **545**, 63
 Euclid Collaboration, Barnett, R., Warren, S. J., et al. 2019, *A&A*, **631**, A85
 Fan, X., Carilli, C. L., & Keating, B. 2006a, *ARA&A*, **44**, 415
 Fan, X., Strauss, M. A., Becker, R. H., et al. 2006b, *AJ*, **132**, 117
 Fan, X., Strauss, M. A., Schneider, D. P., et al. 2001, *AJ*, **121**, 54
 Feng, Y., Croft, R. A. C., Di Matteo, T., & Khandai, N. 2013, *MNRAS*, **429**, 1554
 Furlanetto, S. R., & Oh, S. P. 2005, *MNRAS*, **363**, 1031
 Furlanetto, S. R., Oh, S. P., & Briggs, F. H. 2006, *PhR*, **433**, 181
 Geil, P. M., & Wyithe, J. S. B. 2009, *MNRAS*, **399**, 1877
 Geil, P. M., Wyithe, J. S. B., Petrovic, N., & Oh, S. P. 2008, *MNRAS*, **390**, 1496
 Ghara, R., Choudhury, T. R., & Datta, K. K. 2016, *MNRAS*, **460**, 827
 Ghara, R., Choudhury, T. R., Datta, K. K., & Choudhuri, S. 2017, *MNRAS*, **464**, 2234
 Graziani, L., Ciardi, B., & Glatzle, M. 2018, *MNRAS*, **479**, 4320
 Graziani, L., Maselli, A., & Ciardi, B. 2013, *MNRAS*, **431**, 722
 Hassan, S., Liu, A., Kohn, S., & La Plante, P. 2019, *MNRAS*, **483**, 2524
 Hinshaw, G., Larson, D., Komatsu, E., et al. 2013, *ApJS*, **208**, 19
 Kakiichi, K., Graziani, L., Ciardi, B., et al. 2017, *MNRAS*, **468**, 3718
 Khandai, N., Di Matteo, T., Croft, R., et al. 2015, *MNRAS*, **450**, 1349
 Kulkarni, G., Keating, L. C., Haehnelt, M. G., et al. 2019, *MNRAS*, **485**, L24
 Ma, Q., Ciardi, B., Eide, M. B., & Helgason, K. 2018, *MNRAS*, **480**, 26
 Madau, P., Meiksin, A., & Rees, M. J. 1997, *ApJ*, **475**, 429
 Majumdar, S., Bharadwaj, S., Datta, K. K., & Choudhury, T. R. 2011, *MNRAS*, **413**, 1409
 Mao, Y., Shapiro, P. R., Mellema, G., et al. 2012, *MNRAS*, **422**, 926
 Maselli, A., Ciardi, B., & Kanekar, A. 2009, *MNRAS*, **393**, 171
 Maselli, A., Ferrara, A., & Ciardi, B. 2003, *MNRAS*, **345**, 379
 Moriwaki, K., Yoshida, N., Eide, M. B., & Ciardi, B. 2019, *MNRAS*, **489**, 2471
 Mortlock, D. J., Warren, S. J., Venemans, B. P., et al. 2011, *Natur*, **474**, 616
 Patil, A. H., Yatawatta, S., Koopmans, L. V. E., et al. 2017, *ApJ*, **838**, 65
 Patil, A. H., Zaroubi, S., Chapman, E., et al. 2014, *MNRAS*, **443**, 1113
 Planck Collaboration, Aghanim, N., Akrami, Y., et al. 2018, arXiv:1807.06209
 Rosenfeld, A., & Pfaltz, J. L. 1966, *JACM*, **13**, 471
 Ross, H. E., Dixon, K. L., Ghara, R., Iliev, I. T., & Mellema, G. 2019, *MNRAS*, **487**, 1101
 Ross, H. E., Dixon, K. L., Iliev, I. T., & Mellema, G. 2017, *MNRAS*, **468**, 3785
 Seiler, J., Hutter, A., Sinha, M., & Croton, D. 2018, *MNRAS*, **480**, L33
 Shimabukuro, H., Yoshiura, S., Takahashi, K., Yokoyama, S., & Ichiki, K. 2017, *MNRAS*, **468**, 1542
 Springel, V. 2005, *MNRAS*, **364**, 1105
 Trac, H., & Cen, R. 2007, *ApJ*, **671**, 1
 van Haarlem, M. P., Wise, M. W., Gunst, A. W., et al. 2013, *A&A*, **556**, A2
 Vrbancic, D., Ciardi, B., Jelić, V., et al. 2016, *MNRAS*, **457**, 666
 Watkinson, C. A., Giri, S. K., Ross, H. E., et al. 2019, *MNRAS*, **482**, 2653
 Wilson, T. L., Rohlfs, K., & Hüttemeister, S. 2009, Tools of Radio Astronomy (Berlin: Springer)
 Wyithe, J. S. B., & Loeb, A. 2004, *ApJ*, **610**, 117

Zawada, K., Semelin, B., Vonlanthen, P., Baek, S., & Revaz, Y. 2014,
[MNRAS](#), **439**, 1615